university of groningen

faculty of science and engineering

Investigation of the wideband mass accuracy of an MRTOF spectrometer

Dominika Widera

university of groningen

faculty of science and engineering

University of Groningen

Investigation of the wideband mass accuracy of an MRTOF spectrometer

Bachelor's Thesis

To fulfill the requirements for the degree of
Bachelor of Science in Physics
at University of Groningen under the supervision of
Prof. dr Julia Even.
and
Prof. dr. Peter Schury

Dominika Widera (s5260426)

July 9, 2025

Contents

Acknowledgments

I would like to extend my sincere gratitude to everyone who played a role in helping me complete this thesis. I would like to extend my special thanks to my thesis supervisors, Prof. Dr. Julia Even and Prof. Dr. Peter Schury, for their invaluable guidance throughout this journey. I would also like to express my gratitude to Dr. Marco Rosenbusch for guiding me through the research process and sharing his insights into the world of science. I am also grateful to the RIKEN Research Institute for access to equipment and essential resources that made my research possible.

Abstract

This thesis investigates the wideband mass accuracy of the Multi-Reflection Time-of-Flight Mass Spectrometer (MRTOF-MS) at the RIKEN Nishina Center, focusing on systematic uncertainties. A source of curium-248 (Cm-248) is used to study the spectrometer's precision across a broad mass-to-charge range (A/q = 44–133). Rubidium-85 (Rb-85) is used as mass reference mass, while calibration of the spectrometer's offset time is performed once using caesium-133 (Cs-133). Calibration with Cs-133 yielded an optimal time offset of 195.6 nanoseconds, whera the relative mass deviations remained consistently within $\pm 2.1 \times 10^{-6}$ for most ion species, when the same offset time was used for all measurements. The lighter ions with mass-to-charge ratio (A/q = 44-75) have been found to exhibit larger discrepancies in accuracy as they are further away from the reference ion. Purified ion spectra of a chosen mass number have been obtained using the in-MRTOF deflector method. The capability of the MRTOF-MS to identify species in broad-band mode is confirmed. The study is basis for a further improvement, as it clarifies the order of magnitude of a previously expected but uncertain problem. Suggestions for future work are advanced calibration techniques, improved field stability, and real-time correction algorithms.

Keywords: MRTOF-MS, mass accuracy, wideband spectrometry, nuclear physics, Cm-248 fission products

1 Introduction

Nuclear physics has long been a cornerstone of modern scientific research, driving significant discoveries in various fields of human knowledge. It enables us to understand both the fundamental constituents of the universe, such as nuclear shell interactions and decay processes and the vast phenomena associated with stellar dynamics [1]. Studies of exotic nuclei far from stability provide insight into the evolution of nuclear structure along the chart of nuclides, as well as crucial input for modelling astrophysical processes. Precision mass measurements of these nuclei provide direct access to the nuclear binding energy, thereby serving as benchmark data to test nuclear models, such as the shell model or liquid drop model [2]. To achieve this, various advanced measurement systems have been developed, including Penning traps and Time-of-Flight Mass Spectrometers (TOF MS). Among these advanced techniques is the Multi-Reflection Time-of-Flight Mass Spectrometer (MRTOF-MS). Recent advancements show that both MRTOF-MS and Penning traps can achieve a mass resolution of $R > 100,000$ within timescales of less than 10 ms [3] [4]. MRTOF-MS works on the principle of extending the time-of-flight of an ion by trapping it inside an electrostatic field, where it reflects back and forth [5]. This straightforward mechanism contrasts with the more complex double-trap systems used by Penning traps, which require more pre-cooling and preparation steps for ions before measurement [4]. The workings of MRTOF-MS are much simpler, therefore demanding less time. This enables mass determinations of superheavy elements ($Z \geq 100$) previously inaccessible to conventional techniques [6]. This method holds significant promise for addressing challenges related to wideband accuracy across diverse mass ranges (A/q=20-300) [6].
An advanced MRTOF-MS is operational at the RIKEN Nishina Centre in Wakō, Japan. This facility plays a vital role in advancing the fields of nuclear and particle physics, facilitating detailed investigations into isotopic compositions and reactions. However, like every experimental method, RIKEN's MRTOF-MS introduces inaccuracies due to systematic errors, such as calibration drift or unstable electrostatic drift, and necessitates trade-offs between resolution, mass range, and measurement time [3].
In this context, the spontaneous fission decay products of curium-248 are being analyzed to evaluate the wideband mass accuracy achievable with RIKEN's MRTOF spectrometer. Cm-248's spontaneous fission yields ions across A/q = 40–160, providing an ideal test bench to quantify systematic errors. Instrument-specific biases are isolated by comparing results to the Atomic Mass Evaluation (AME) [7]. Addressing the inaccuracies introduced by the MRTOF system will be essential for fully understanding and resolving these underlying issues moving forward.
To summarise, this thesis focuses on the following problem:

Q1. How large is the systematic mass uncertainty of the system for wideband measurements?

The thesis includes a comprehensive review of the background literature to elucidate the theoretical framework. It also shows the operation of the MRTOF system and its inherent limitations. A detailed methodology section outlines the experimental setup and describes the procedures employed, followed by results and a conclusion. Supplementary raw data are provided in the appendix for reference and verification.

2 Background Literature

Multi-reflection time-of-flight mass spectrometry (MRTOF-MS) achieves ultra-high mass resolution by trapping ions in an electrostatic mirror system. This technique relies on a few principles described in the sections below.

2.1 Multi-Reflection Time-of-Flight Spectrometry

The Multi-Reflection Time-of-Flight Spectrometer (MRTOF) is designed to precisely measure the time-of-flight of nuclei, achieving high accuracy in mass spectrometric analysis. Various configurations of time-of-flight mass spectrometry (TOF-MS) exist, including linear, multi-reflection, multi-turn, and ion-trap coupled TOF-MS systems. In Multi-Reflection Time-of-Flight Mass Spectrometry, ions are injected into an electrostatic ion trap consisting of two or more mirrors [5]. These mirrors establish an electrostatic field that enables the continuous reflection of ions, allowing them to travel back and forth within the trap. The resulting increase in the ions' time-of-flight leads to improved mass resolution by accumulating the slight variations in ion transit times, thereby significantly improving the sensitivity and accuracy of mass measurements [5].
The fundamental operating principle of the MRTOF mass spectrometer is predicated on the concept of time-of-flight (TOF), which is intricately linked to the mass-to-charge ratio (A/q) of the ions. The TOF integral for N reflections along a specified path, denoted as z, can be expressed in terms of the potential $\phi(z)$ at position z:

$$t = N \oint \frac{\mathrm{d}z}{v(z)} = N \int_{z_1}^{z_2} \frac{\mathrm{d}z}{\sqrt{2(q/m)(\Phi_0 - \Phi(z))}}, \tag{1}$$

where $v(z)$ is the position-dependent speed of the ion under the influence of an electric potential. The Equation 1 can be simplified to show that it is proportional to the square root of the mass-to-charge ratio of the ions traversing the path [6].

$$t = 2N\sqrt{\frac{m}{q}} \int_0^{z_0} \frac{\mathrm{d}z}{\sqrt{2(\Phi_0 - \Phi(z))}} \tag{2}$$

Therefore, it yields a simple solution of,

$$t = k\sqrt{\frac{m}{q}}, \tag{3}$$

where, k is a constant as the potential $\Phi(z)$ in the integral from the Equation 2 stays the same inside specific system. It is derived from the specific design parameters and operational characteristics of the MRTOF device [5].
Implementing multiple ion reflections within the mass spectrometer enhances the overall time-of-flight, significantly amplifying subtle discrepancies in mass-to-charge ratios (A/q). Conversely, with the precise calibration of the mirror electric fields, ions with identical m/q values can be directed to arrive at the detector simultaneously [3]. The mass resolution (R) is given by,

$$R = \frac{m}{\Delta m} = \frac{t}{2\Delta t} \tag{4}$$

where Δt is the spread in arrival times. In the case of MRTOF-MS, the mass resolution (R) is proportional to the number of reflections, enabling the potential for resolutions that exceed $R = 10^5$ under optimal conditions [5].

2.2 Optimization of Time-of-Flight Measurements

The MRTOF-MS utilises electrostatic fields and ion mirrors to measure nuclear masses accurately. Ions are confined within an electrostatic potential well created by two ion mirrors, enabling multiple reflections that increase their time-of-flight. They make a static potential barrier [8]. The ion's motion within this potential well is governed by its kinetic energy, which in turn determines the period of oscillation. The potential energy diagram (Figure 1) depicts the axial potential distribution $\Phi(z)$ inside an MRTOF mirror trap. The potential increases after an ion falls into a potential well, forcing it to bounce back, as it cannot overcome the barrier. The ion will continue to oscillate within the field until the potential at the boundary is lowered, allowing it to escape the field.
A relationship can describe the ion's kinetic energy,

$$E < q \cdot \Phi_{max} \tag{5}$$

where q is the charge of the ion. If the ion's kinetic energy is not greater than the two maxima of the potential (injection/ejection side), it is not going to escape [8].

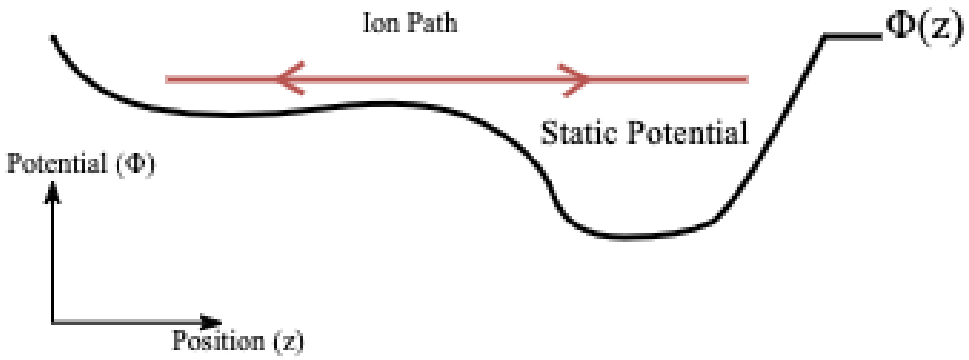

Figure 1: A schematic showing a static (non-time-varying) potential wall that reflects ions. Ions enter from the field, lose kinetic energy climbing the potential slope, and are reflected back.

To achieve high-precision time-of-flight measurements, the MRTOF mirrors are tuned to compensate for variations in kinetic energy. This negative time dispersion ensures that ions of slightly different energies arrive at the detector simultaneously [8]. To ensure an accurate measurement of time of flight and, therefore, mass, a special mechanism for time focusing is needed [3]. Ions lose kinetic energy δE_k proportional to their penetration depth into the potential slope. The Figure 2 demonstrates how ions with different kinetic energies travel inside the static potential after their first lap. The objective is to optimise the arrangement of mirrors within the MRTOF device to ensure that all ions complete their respective trajectories simultaneously, as illustrated in Figure 2, corresponding to N laps.

$$\frac{\delta T}{\delta E_k} = 0, \tag{6}$$

where T is the total time of flight. In theory, perfect time focusing is achieved when the relationship from the Equation 6 holds true. However, in practice, ions require multiple laps to be focused. Therefore, a mirror configuration is chosen that introduces negative time dispersion, gradually aligning ion arrival times over many reflections. Higher-energy ions penetrate deeper, resulting in a longer flight path with each reflection [8]. As mentioned above, this can be mitigated by correcting the trajectory with a mirror setup. Mathematically, it means that the result of the Equation 6 should be negative [8].

The combination of static trapping and energy-compensated time focusing leads to enhanced mass resolution and increased measurement precision [8]. This approach facilitates the separation of isobaric species, such as rare isotopes that differ by sub-ppm mass differences and reduces sensitivity to initial beam energy variations, enhancing the overall analysis [8].

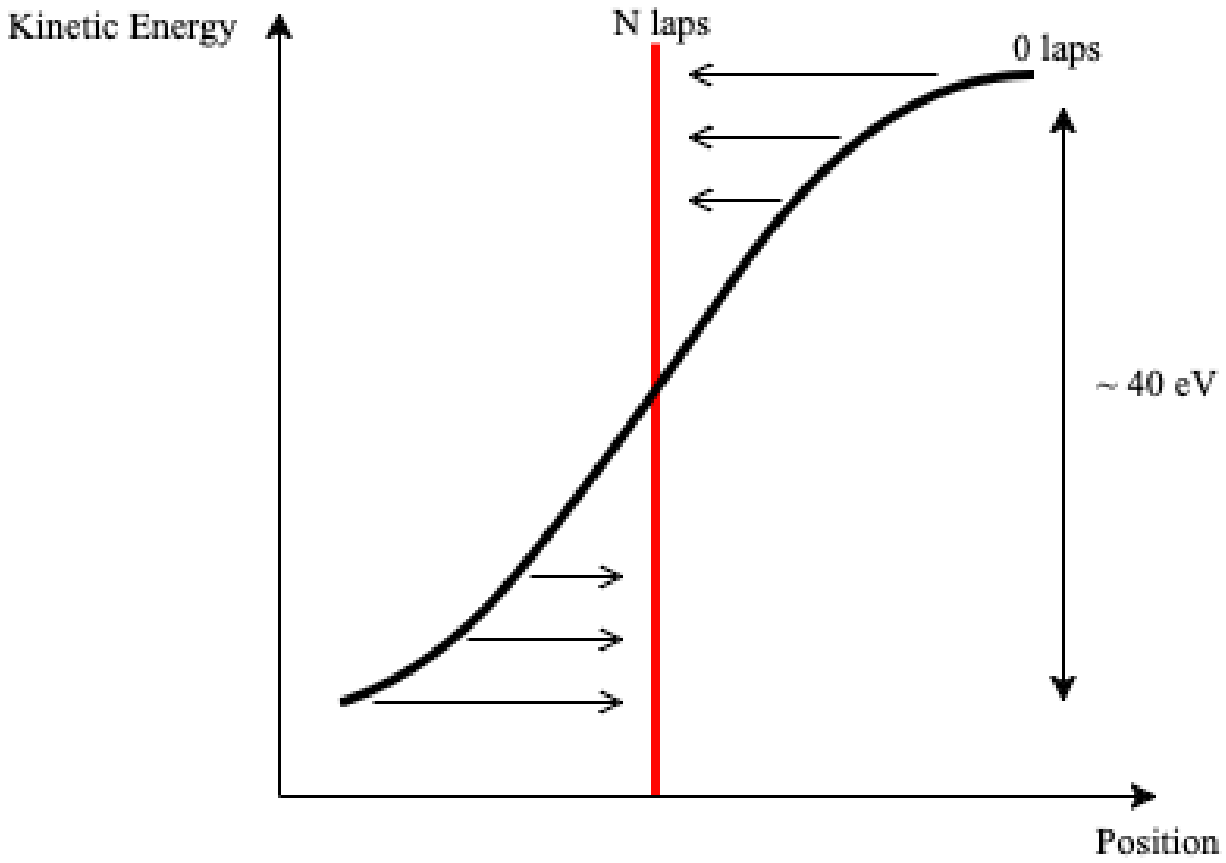

Figure 2: A schematic showing the energy spread between ions. The ions do not lose energy during reflections; those with higher initial kinetic energy travel deeper into the mirror potential. This leads to a longer path and slower average speed, which compensates for their energy advantage.

3 Methodology

The methodology section outlines the experimental and analytical approaches employed to measure the mass of fission products of Curium-248 (Cm-248) using the Multi-Reflection Time-of-Flight Mass Spectrometer at RIKEN's RIBF facility. The experimental setup comprises three main components: ion accumulation and cooling, ion transport and energy adaptation, and the MRTOF-MS system for mass analysis. Key techniques include ion trapping, time-of-flight measurement, and precise ion filtering using an in-MRTOF deflector (Section 3.1 and 3.2). Data analysis was performed using the ROOT framework and ToolPackage5_v2, with mass deviations calculated relative to the Atomic Mass Evaluation (AME) (Section 3.3). The methodology section outlines the procedures for ensuring high-resolution measurements and statistical significance, supported by calibration with reference ions such as Rb-85 and Cs-133.

3.1 Experimental Setup

The MRTOF-MS experiment setup is in the RIBF facility in RIKEN, Japan. The experimental setup is pictured below (Figure 3). The setup diagram is not to scale.
We can differentiate three different sections of the setup. The first section accumulates and cools the ions. The following section transports the ions and adapts their energy to the required by MRTOF itself. The last section is the MRTOF-MS itself that analyses the mass [3].

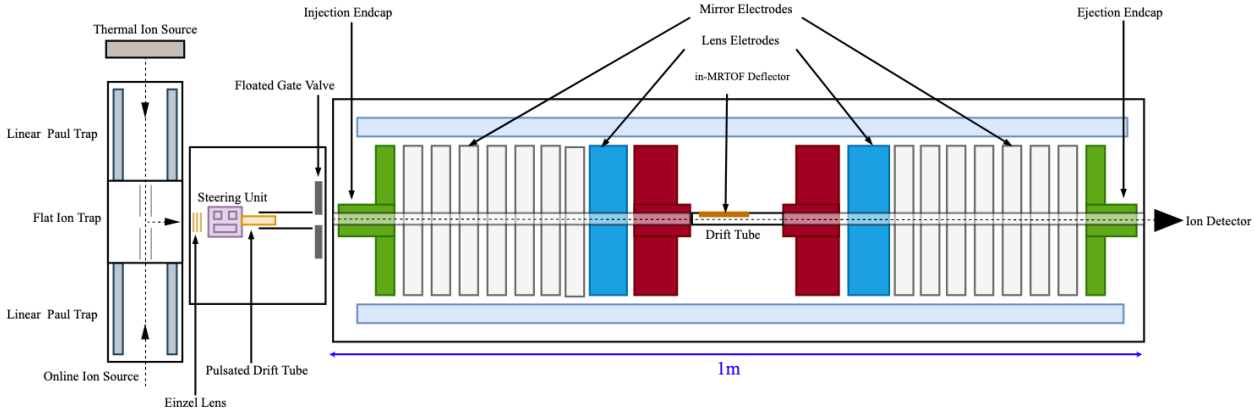

Figure 3: Schematic diagram of the MRTOF-MS setup at RIKEN's RIBF facility, as described in Rosenbusch et al. (2023) [3]. Not to scale. This setup is designed for high-precision mass measurements of radioactive nuclei produced at the RIBF.

The radioactive source utilised in this study is curium-248, with a measured activity of 10 kilobecquerels (10 kBq). This source undergoes spontaneous fission with a percentage of 8.39%, whereas the rest of the decay mode is an alpha decay [9]. The resulting fission fragments recoil from the Cm-248 target and are subsequently captured in a gas cell. The exact mechanism of combining fission source and gas cell is outside the scope of this thesis. It has been described in detail by *Kimura et al.* in their comprehensive study of ^{252}Cf fission fragments [10]. Ions are then guided into the MRTOF system via radiofrequency carpets and electric fields, processed through the online ion source [3]. A thermal source generates rubidium-85, a type of alkali ion, to to provide a well-known mass reference.
Both the curium and rubidium sources continuously inject ion beams through the Paul traps, with subsequent transfers occurring cycle by cycle to the Flat trap. After cooling in the Flat Trap, the

ions are ejected and focused by an Einzel lens (three 3-mm-thick plates) before entering the MRTOF spectrometer [3]. The ions move through a steering unit and a pulsed drift tube (PDT) for their time-of-flight measurement. The PDT enhances the energy of the ions, allowing them to move between the mirror electrodes without requiring high voltage to be applied to the ion trap [3]. The ions are confined along the axis within the MRTOF-MS by rapidly changing the bias applied to the injection endcap, which is the first mirror electrode. They travel a set number of laps inside the drift tube.

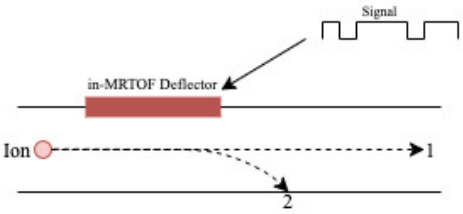

Figure 4: Schematic of the in-MRTOF deflector. **(1)** Ion path when the deflector is off (no deflection). **(2)** Ion path when the deflector is active (deflection into the drift tube).

This experiment focuses on high-accuracy mass measurements, requiring precise ion filtering. The MRTOF-MS system achieves this using an in-MRTOF deflector. Besides improving the resolution and reducing the noise, it either deflects an ion that is not part of the measurement or allows it to bounce back and forth. For example, if the measurement is focused on measuring a mass-to-charge ratio of 100, any other ion with a different mass-to-charge ratio will be deflected. The in-MRTOF deflector can be either turned on or off. While it is being turned off, the ions can safely follow the path of their flight (as seen in the Figure 4, described with *1*). However, when it is turned on, the ions deflect into the drift tube, so they cannot be measured (as seen in the Figure 4, described with *2*). The space between mirrors, where the deflector is placed, is kept at a stable potential to increase the accuracy of the measurement.
At the end of the flight, the ions are directed at the detector, where the measurement data is taken and stored.

3.2 Experimental Methods

To ensure precise mass determination, a MRTOF analysis was performed across all mass spectra, focusing on regions exhibiting both high and low counts per second (cps). Known masses spanning a wide range of intensities were selected to validate the MRTOF's accuracy. Ions underwent 680 laps within the MRTOF system, enhancing separation efficiency and mass-resolving power. Measurements continued until statistically significant peaks were observed, requiring over 1,000 events for high cps and ideally over 500 for low cps. Total measurement times ranged from 30 minutes to 48 hours, depending on the mass number and count rate.
The in-MRTOF deflector (described in Section 3.1) was employed to selectively filter ions outside the target A/q range, ensuring only relevant species reached the detector. The detected ions were predominantly singly ($q = 1+$) or doubly charged ($q = 2+$), their identification follows a standard convention of the mass-to-charge ratio (A/q). Twenty-one measurements have been taken across different mass-to-charge ratios.

3.3 Data Analysis Methods

All measurements acquired using the MRTOF-MS were analysed using ROOT, a high-energy physics data analysis framework developed by CERN. For data processing, I employed ToolPackage5_v2 [11], an open-source software suite available on GitHub (https://github.com/MaiDo2018/toolpackage5_v2). The uncertainties in TOF and the resulting mass values were calculated automatically by ToolPackage5 based on the fit quality and internal propagation of errors. Therefore, they are not manually

derived in this thesis.
From the Equation 3, we can see that the ratio of TOFs is,

$$\frac{t_1 - t_0}{t_2 - t_0} = \sqrt{\frac{m_1 q_2}{m_2 q_1}} \tag{7}$$

where t_0 is the offset time (described in Section 4.1), t_1 and t_2 are TOFs for an unknown ion and a calibration source, q_1 and q_2 are their respective charges, and m_1 and m_2 are their respective masses. The equation above facilitates the analysis of the relationship between the masses of ions and their time of flight.
The results from the experimental data have been analysed using the relative mass deviation formula,

$$\Delta m = \frac{m_{AME} - m_{exp}}{m_{AME}} \tag{8}$$

where m_{AME} is the mass value from the Atomic Mass Evaluation [7] and m_{exp} is the experimental mass measurement. A positive Δm indicates that our measurements are underestimated, while a negative Δm suggests an overestimation.
An uncertainty calculation was also performed, yielding,

$$\delta\Delta m = \sqrt{(\frac{m_{exp}}{m_{AME}^2} \cdot \delta m_{AME})^2 + (-\frac{\delta m_{exp}}{m_{AME}})^2} \tag{9}$$

for an absolute uncertainity, where δm_{AME} is the uncertainty provided by the Atomic Mass Evaluation [7] and δm_{exp} is the uncertainty of the measurement. For relative uncertainty, the following formula was calculated.

$$\frac{\delta\Delta m}{\Delta m} = \frac{1}{1 - \frac{m_{exp}}{m_{AME}}} \sqrt{(\frac{m_{exp}}{m_{AME}} \frac{\delta m_{AME}}{m_{AME}})^2 + (\frac{\delta m_{exp}}{m_{exp}})^2} \tag{10}$$

4 Results

The results section presents the findings from the investigation into the wideband mass accuracy of the Multi-Reflection Time-of-Flight spectrometer. This section is divided into two main parts: the calibration of the measurements and the analysis of mass measurement accuracy.

4.1 Calibration of the Measurements

To ensure the precise calibration of the data corresponding to the initial time t_0, the well-established mass of caesium-133^{1+} was employed as a reference. A series of starting times for the time-of-flight of Cs-133^{1+} were tested, with the results summarised in Table 1 and graphically illustrated in Figure 5. The relative mass difference was computed using Equation 8 to evaluate the accuracy of each trial value. The optimal calibration time yielded the least deviation between the experimentally processed mass and the literature AME value [7]. In this case, the best agreement occurred at 195.6 nanoseconds.

To quantify the uncertainty in this calibration, upper and lower bounds were calculated using a relative mass difference formulation, defined as:

$$\Delta m_{\text{lower}} = \frac{m_{\text{AME}} - m_{\text{exp}} - \Delta m_{\text{exp}}}{m_{\text{AME}}} \tag{11}$$

$$\Delta m_{\text{upper}} = \frac{m_{\text{AME}} - m_{\text{exp}} + \Delta m_{\text{exp}}}{m_{\text{AME}}} \tag{12}$$

where Equation 11 provides the lower-bound uncertainty and Equation 12 gives the upper-bound uncertainty. As depicted in Figure 5, these bounds result in a calibration uncertainty of approximately 0.6 nanoseconds in the determination of t_0

Table 1: Summary of initial time-of-flight t_0 analysis showing relative mass differences and upper and lower uncertainty bounds.

Initial Time-of-Flight t_0	**Relative Mass Difference** ($\times 10^{-7}$)	Δm_{upper} ($\times 10^{-7}$)	Δm_{lower} ($\times 10^{-7}$)
187.0	1.91	1.73	2.08
190.0	1.24	1.06	1.40
195.0	0.132	-0.044	0.309
195.2	0.881	0.887	0.265
195.5	0.0216	-0.177	0.176
195.6	-0.000602	-0.177	0.176
195.8	-0.00228	-0.200	0.154
197.0	-0.311	-0.488	-0.134

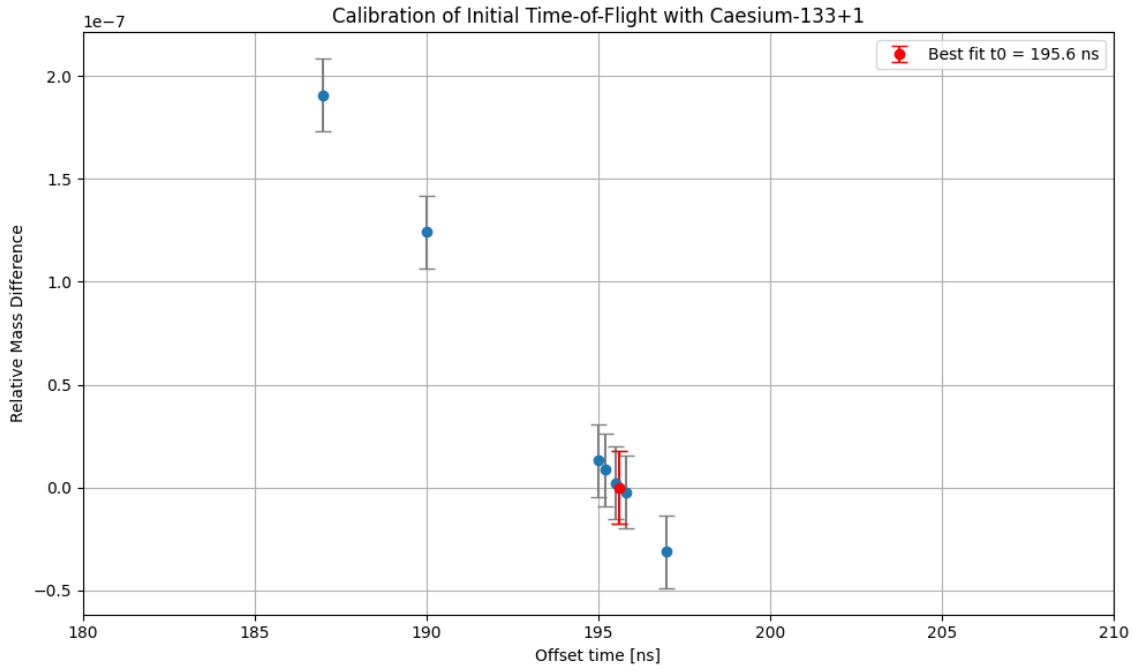

Figure 5: Calibration of the initial time-of-flight parameter (t_0) using measurements with $^{133}Cs^{1+}$. The plot shows the relative mass difference as a function of the initial time-of-flight value. Error bars represent the asymmetric uncertainties derived from upper and lower bounds. The red point highlights the best-fit t_0 value at 195.6 ns, corresponding to the minimum mass difference and its associated uncertainty.

4.2 Mass Measurement Accuracy

The mass measurement accuracy of the MRTOF spectrometer was assessed using a range of ion species, from light molecules like CO_2^{1+} to heavy isotopes such as Cs-133^{1+}. An example of the measured spectrum, displaying the peak of the ion at a mass-to-charge ratio of A/q = 110, is presented in Figure 6. All of the spectra are attached in the Appendix (Section B).

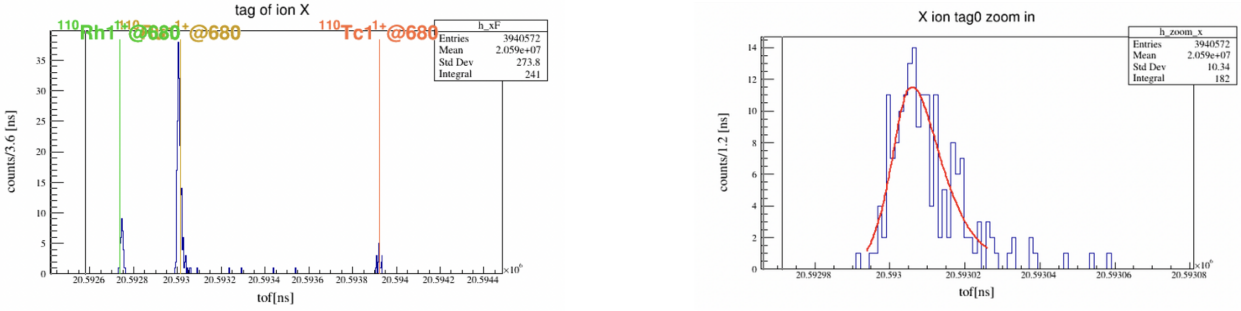

(a) The overview of measured ions for fitting.

(b) Fitted peak of $^{110}Ru^{1+}$.

Figure 6: Figures above show the peaks measured of mass-to-charge ratio A/q=110. Subfigure (**a**) shows all the peaks available. Subfigure (**b**) shows the fitted peak of $^{110}Ru^{1+}$. Other peaks are discarded due to low count rate.

The relative mass differences were calculated using Equation 8. At the same time, uncertainties were

determined using Equation 9 for absolute uncertainty and Equation 10 for relative uncertainty. The results, presented in Table 2, demonstrated a consistent measurement trend, with most deviations falling within a narrow range. As illustrated in Figure 7, the plotted points reflect these findings.
Most of the measured species displayed a negative relative mass difference (see Table 2), suggesting a systematic overestimation of their masses. Lighter ions (with A/q ratios ranging from 44 to 75) exhibited greater discrepancies, resulting in an order-of-magnitude difference. In contrast, masses closer to the references (Rb-85 and Cs-133) tend to show higher accuracy, with negligible associated errors.
A fundamental assumption in MRTOF-MS theory is the presence of perfectly static electric fields within the ion optical system [12]. However, as Wollnik noted, ”the assumption of perfectly stable electrostatic fields represents an oversimplification that fails to account for several practical considerations in real spectrometer operation.” [12]. The high-voltage power supplies generating mirror potentials exhibit short-term ripple (for short-term measurements at high cps) and long-term drift (for long-term measurements at low cps). These fluctuations directly impact the isochronous condition [13], where field stability is crucial for maintaining time-focusing. Dielectric charging on the surfaces of insulators results in gradually varying field distortions, which become particularly pronounced during prolonged measurement intervals. The data collected confirm increased drift during long measurements, showing measurable deviations that develop over timescales of several hours [3]. Temperature-dependent changes in electrode geometry and dielectric properties introduce additional field instabilities [6].

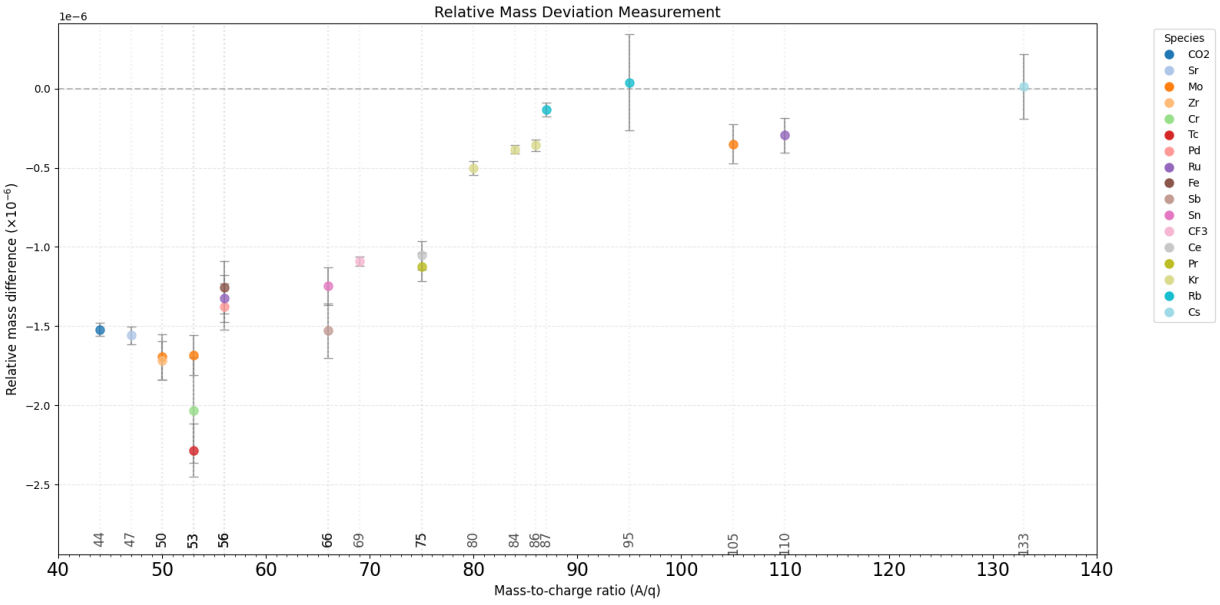

Figure 7: The graph above shows the relative mass deviation for different species of ions. The relative mass difference has been calculated with Equation 8. On the right side, there is a legend showing ion species present on the graph.

Low-cps ions require prolonged measurements, which significantly increases the uncertainty, for example, Cr-53 or Rb-95. The detailed list of counts per ion is in the Table 4, found in the Appendix (Section B). Some results were deemed inadmissible due to low count rates, where the systematic error was too significant to consider them reliable.
As illustrated in Figure 7, the majority of the results demonstrate high precision, indicated by the clustering of measurements. However, it is visible that one mass-to-charge ratio deviates from this

trend. The results from A/q=53 are technetium-106, molybdenum-106 (both doubly charged, $q = +2$) and chromium-53 (singly charged, $q = +1$).
One additional measurement of A/q = 53 was performed, but with an increased number of laps at 710 laps. The accompanying figure (Figure 8) illustrates the relative mass difference between molybdenum-106 and technetium-106 as a function of the number of laps. The method used to determine the results follows the same rigour as above. The relative mass difference was calculated using Equation 8, and the associated uncertainty was determined utilising Equation 9. The data indicate that the results remain consistent across varying lap counts, suggesting that the initial measurement at 680 laps is unlikely to have involved significant error. The counts for Mo-106^{2+} and Tc-106^{2+} in the first measurement were 1044 and 419, respectively, while in the subsequent measurement, the counts were 128 for Mo-106^{2+} and 366 for Tc-106^{2+}. Given the results from Figures 7 and 8, an isobaric calibration was performed to obtain the mass ratio between the two isotopes directly.

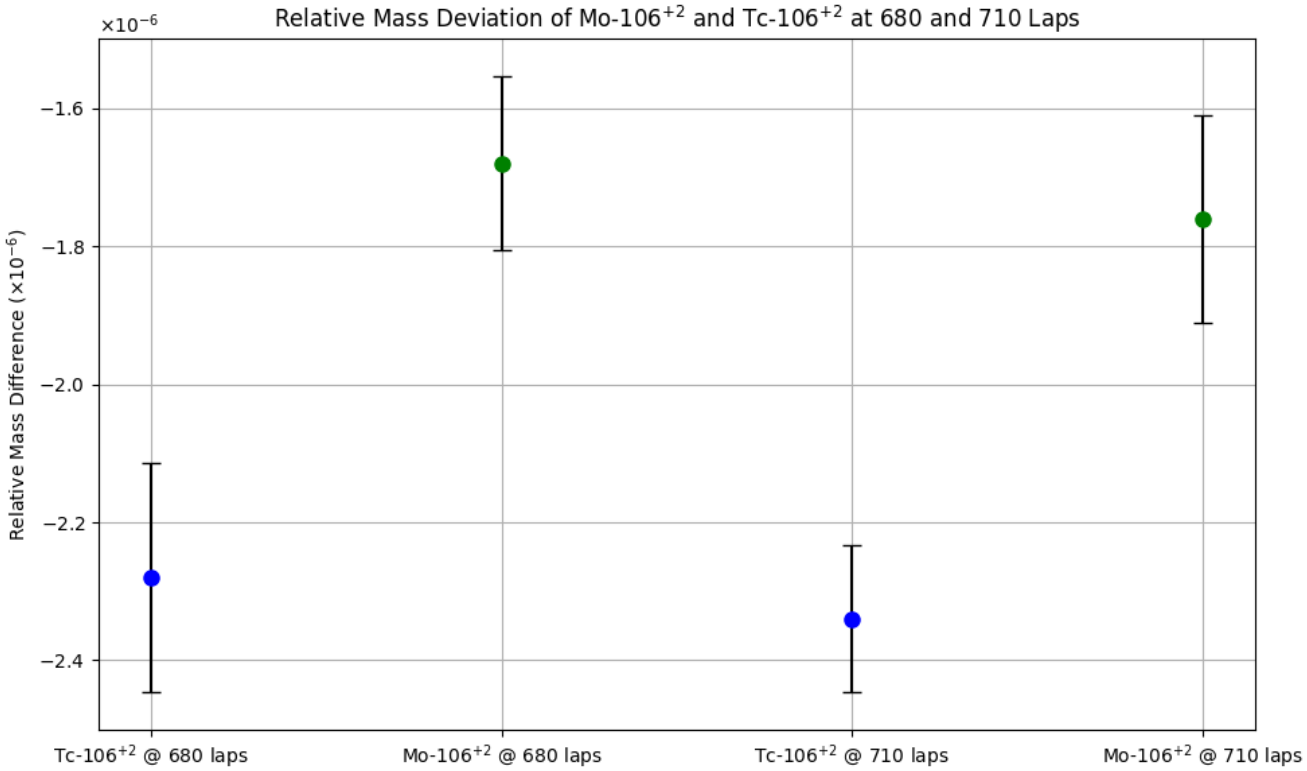

Figure 8: The graph above shows the relative mass deviation for Tc-106^{2+} and Mo-106^{2+} at 680 and 710 laps. The relative mass difference has been calculated with Equation 8.

The mass of technetium-106 was calculated using molybdenum-106 as a reference. It was found that the mass of Tc-106^{2+} is $m = 105.9144331$ amu at 680 laps and $m = 105.9144301$ amu at 710 laps, yielding a deviation of $7.2 \cdot 10^{-7}$from the AME mass [7]. The figure shows the mass difference between the experimental mass and the AME mass. The weighted average of the mass deviation was determined to be 70.21 keV, with an uncertainty of 12.34 keV, corresponding to a significance of 5.69σ. Consequently, it is highly unlikely that this result is a product of random statistical fluctuations. The relative weighted average difference was calculated at 0.712 ppm, with an uncertainty of 0.125 ppm, indicating a higher-than-average discrepancy between this result and the AME findings.
A review of the AME2020 data reveals that the evaluated masses of Tc-106^{2+} and Mo-106^{2+} are not primarily based on recent, direct measurements [7]. Instead, they depend on historical measurements,

many of which are indirect or based on intermediate references. For Mo-106^{2+}, earlier mass values were connected through a chain of decay and reaction Q-values involving nuclides like Zr-97^{2+} and Nb-97^{2+}, many of which were measured via beta-decay [14]. Concisely, Tc-106^{2+} was evaluated using Penning trap data on Rh-102^{2+}, which is itself tied to Ru-102^{2+} through (p,n) and (d,p) reactions [15]. Both Zr-97^{2+} and Rh-102^{2+} have known isomeric states, and uncertainties in assigning these states correctly in earlier experiments may have introduced systematic biases. To ensure the validity of my results, additional measurements must be conducted across different lap numbers and with a higher count number.

Figure 9: The graph above shows the isobaric calibration of Tc-106^{2+} with a reference Mo-106^{2+} at 680 and 710 laps. The red shaded region is the weighted average of the isobaric calibration with a corresponding uncertainty. The grey shaded region is the AME value with its uncertainty [7].

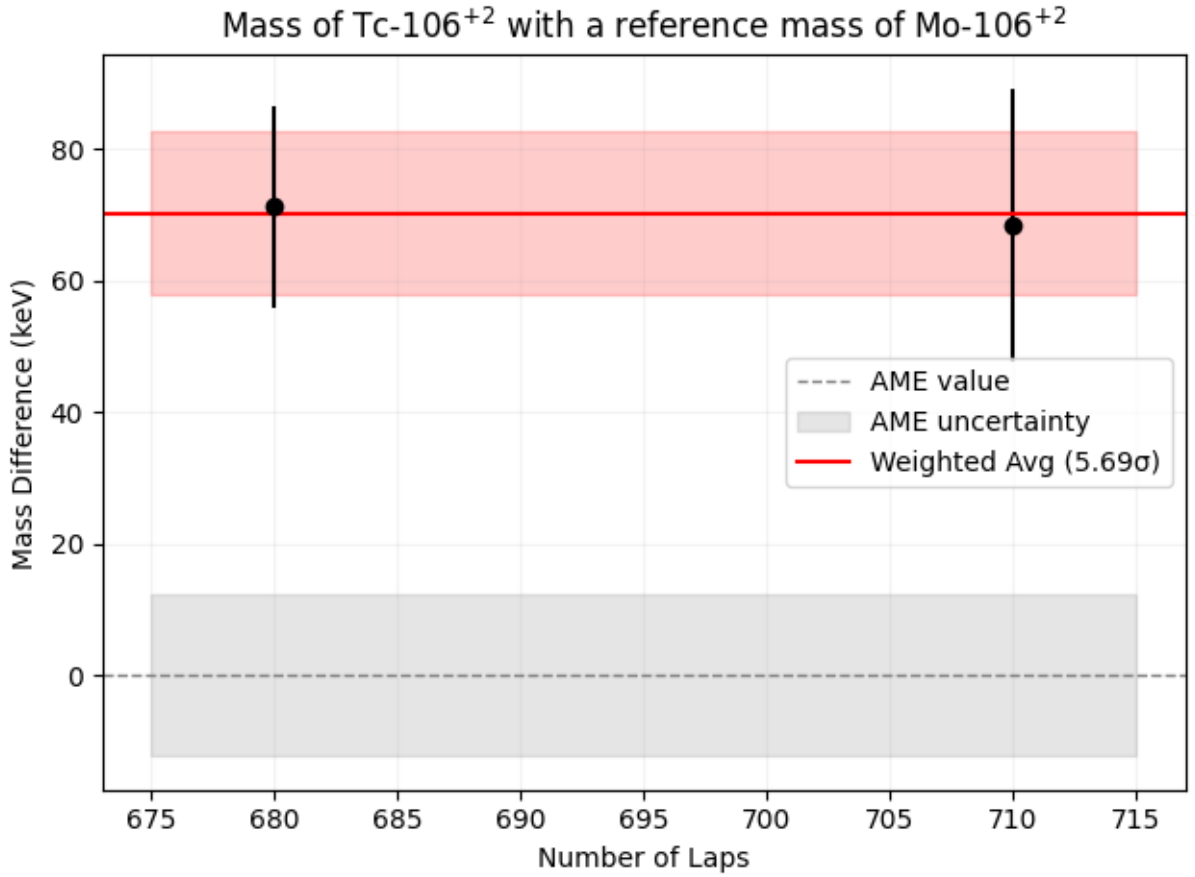

Table 2: Summary of mass measurement results showing relative mass differences (in amu), total uncertainties, and relative uncertainties for various isotopes.

Species	**Relative mass difference** ($\times 10^{-6}$)	**Absolute uncertainty** ($\times 10^{-6}$)	**Relative uncertainty**
CO_2^{+1}	-1.5217	0.0422	0.0277
Sr-94^{2+}	-1.5570	0.5731	0.3680
Mo-100^{2+}	-1.6935	0.5224	0.3086
Zr-100^{2+}	-1.7165	0.5117	0.2938
Cr-53^{+}	-1.2456	0.4425	0.3552
Tc-106^{2+}	-2.0959	0.4476	0.2136
Mo-106^{2+}	-1.3425	0.4437	0.3305
Pd-112^{2+}	-1.3759	0.4019	0.2953
Ru-112^{2+}	-1.3273	0.4010	0.3021
Fe-56^{+}	-1.2564	0.3933	0.3130
Sb-132^{2+}	-1.5300	0.2517	0.1645
Sn-132^{2+}	-1.2500	0.2550	0.2040
CF_3^{+1}	-1.0900	0.0274	0.0251
Ce-150^{2+}	-1.0520	0.1121	0.1066
Pr-150^{2+}	-1.1280	0.1230	0.1090
Kr-80^{+}	-0.5018	0.0588	0.1172
Kr-84^{+}	-0.3049	0.0287	0.0942
Kr-86^{+}	-0.3578	0.0359	0.1004
Rb-87^{+}	-0.2973	0.3116	1.0480
Rb-95^{+}	0.0398	0.2173	5.4600
Mo-105^{+}	-0.3504	0.1855	0.5295
Ru-110^{+}	-0.2948	0.2102	0.7130
Cs-133^{+}	0.0001	0.2224	16.790

5 Conclusion

This thesis evaluates the accuracy of the current MRTOF-MS setup at RIKEN Nishina Center in Wakō, Japan. The calibration was performed against ceasium-133 with the offset time of 195.6 nanoseconds (Table 1). This led to a relative mass difference of $-0.000602 \cdot 10^{-7}$ against the Atomic Mass Evaluation (AME) data [7]. The upper bound uncertainty was $-0.177 \cdot 10^{-7}$, and the lower bound uncertainty was $0.176 \cdot 10^{-7}$.
Different species of ions and molecules were measured for the same reference ion to assess the wideband accuracy. The relative mass accuracy results show a deviation between $2.0959 \cdot 10^{-6}$ and $0.0001 \cdot 10^{-6}$ (against calibration ion, caesium-133) to the mass meansured by the AME [7] (Table 2). The absolute uncertainties vary between $0.0274 \cdot 10^{-6}$ and $0.5731 \cdot 10^{-6}$
The accuracy of measurements collected at greater distances from the source is often reduced. This becomes evident in the mass-to-charge range of 44 to 75, as the source ion has an A/q ratio of 133. The observed deviations, especially for the long measurements, can be attributed to challenges in maintaining a static electric field. Instabilities from power supply ripple may have influenced the spread in mass accuracy. Moreover, the statistical uncertainty depends on counts per second, where ions with more cps tend to have a more precise measurement. Different ion species within the same mass-to-charge ratio A/q values tend to cluster closely together, indicating that MRTOF demonstrates satisfactory precision. An improved understanding of these variables is crucial for enhancing the overall accuracy and reliability of the MRTOF-MS within the broad mass spectrum.
A significant discrepancy was found with the isotopes Mo-106^{2+} and Tc-106^{2+}. The experimental mass for Tc-106^{2+} deviated by $7.2 \cdot 10^{-7}$ from the AME value. With a significance level of 5.69σ, this indicates a potential systematic bias in the AME data for these isotopes. The AME values for Mo-106^{2+} and Tc-106^{2+} are based on historical measurements and indirect methods, such as decay chains and reaction Q-values, which may introduce uncertainties due to isomeric states or other factors. Consistency across different lap counts (680 and 710 laps) further supports the reliability of the MRTOF-MS measurements. This highlights the necessity of direct, high-precision mass measurements to validate and refine existing nuclear mass databases.

5.1 Future Work

While the MRTOF-MS demonstrates high precision for targeted measurements, its wideband accuracy is constrained by systematic effects. Future studies could explore more advanced calibration techniques to mitigate the influence of a not perfectly static electric field. Investigating temperature control and more stable power supplies can significantly reduce measurement drifts and enhance consistency over time. As a truely electrostatic field is extremely hard to achieve, especially for long-term measurements, a real-time correction algorithm could be created and tested against a wideband mass spectrum. To better understand the accuracy error, measuring a broader mass spectrum against various reference masses would be beneficial. To perfect its design and operational protocols, further research could investigate the deflector's performance under varying conditions, such as different ion densities or mass ranges.

Bibliography

[1] P. Schury, M. Wada, Y. Ito, Y. Matsuo, S. Naimi, T. Sonoda, H. Mita, F. Arai, and H. Wollnik, "High-precision mass measurements of radioactive isotopes at the RIKEN Multi-reflection Time-of-flight mass spectrograph," *Nuclear Instruments and Methods in Physics Research Section B: Beam Interactions with Materials and Atoms*, vol. 335, pp. 39–43, 9 2014.

[2] P. Möller, A. J. Sierk, T. Ichikawa, and H. Sagawa, "Nuclear ground-state masses and deformations: Frdm(2012)," *Atomic Data and Nuclear Data Tables*, vol. 109–110, pp. 1–204, 2016.

[3] M. Rosenbusch, M. Wada, and S. e. a. Chen, "The new mrtof mass spectrograph following the zerodegree spectrometer at RIKEN's RIBF facility," *Nuclear Instruments and Methods in Physics Research B*, vol. 541, pp. 447–450, 2023.

[4] S. Eliseev, K. Blaum, M. Block, C. Droese, M. Goncharov, E. Minaya Ramirez, D. A. Nesterenko, Y. N. Novikov, and L. Schweikhard, "Phase-imaging ion-cyclotron-resonance measurements for short-lived nuclides," *Physical Review Letters*, vol. 110, p. 082501, February 2013.

[5] H. Wollnik, "Time-of-flight mass analyzers," *Mass Spectrometry Reviews*, vol. 12, no. 2, pp. 89–114, 1993.

[6] P. Schury, M. Wada, Y. Ito, S. Naimi, T. Sonoda, H. Mita, F. Arai, and H. Wollnik, "A multi-reflection time-of-flight mass spectrograph for short-lived and super-heavy nuclei," *Nuclear Instruments and Methods in Physics Research B*, vol. 295, pp. 1–6, 2012.

[7] M. Wang, W. Huang, F. Kondev, *et al.*, "The AME2020 atomic mass evaluation," *Chinese Physics C*, vol. 45, p. 030003, 2021.

[8] R. N. Wolf, G. Marx, M. Rosenbusch, and L. Schweikhard, "Static-mirror ion capture and time focusing for electrostatic ion-beam traps and multi-reflection time-of-flight mass analyzers by use of an in-trap potential lift," *International Journal of Mass Spectrometry*, vol. 349-350, pp. 123–133, 2013.

[9] National Nuclear Data Center, "NuDat 3.0 Database." https://www.nndc.bnl.gov/nudat/, 2023. Brookhaven National Laboratory. Accessed: 2025-05-28.

[10] S. Kimura, M. Wada, H. Haba, H. Ishiyama, S. Ishizawa, Y. Ito, T. Niwase, M. Rosenbusch, P. Schury, and A. Takamine, "Comprehensive mass measurement study of Cf_{252} fission fragments with MRTOF-MS and detailed study of masses of neutron-rich Ce isotopes," *Phys. Rev. C*, vol. 110, p. 045810, Oct. 2024. Received 7Feb2024; revised 14Aug2024; accepted 23Sep2024.

[11] MaiDo2018, "toolpackage5_v2," 2018. Software for MRTOF-MS data analysis.

[12] H. Wollnik and M. Przewloka, "Time-of-flight mass spectrometers with multiply reflected ion trajectories," *International Journal of Mass Spectrometry and Ion Processes*, vol. 96, no. 3, pp. 267–274, 1990.

[13] W. R. Plass, T. Dickel, and S. Purushothaman, "Multi-reflection time-of-flight mass spectrometry," *International Journal of Mass Spectrometry*, vol. 349-350, pp. 134–144, 2013.

[14] U. Hager, T. Eronen, J. Hakala, A. Jokinen, A. Kankainen, S. Rinta-Antila, and J. Äystö, "Precision mass measurements of neutron-rich molybdenum and technetium isotopes," *Physical Review Letters*, vol. 96, no. 4, p. 042504, 2006.

[15] U. Hager, T. Eronen, J. Hakala, A. Jokinen, A. Kankainen, S. Rinta-Antila, A. Saastamoinen, and J. Äystö, "Precision mass measurements of neutron-rich technetium and ruthenium isotopes with the jyfltrap penning trap," *Physical Review C*, vol. 75, no. 6, p. 064302, 2007.

Appendices

All the necessary raw data is presented in the Appendix. It has two subsections: (**A**) raw data of the calibration with Ceasium-133 and (**B**) raw data of the mass accuracy measurement.

A Raw Data of Calibration of the Measurements

The following Table shows the raw data from the calibration of measurements with Cs-133.

t_0 **(ns)**	m_{ame} **(u)**	m_{EXP} **(u)**	Δm_{AME} **(u)**	Δm_{EXP} **(u)**
187.0	132905451.958	132905426.622	0.008	2.350
190.0	132905451.958	132905435.463	0.008	2.350
195.0	132905451.958	132905450.198	0.008	2.350
195.2	132905451.958	132905451.671	0.008	2.350
195.4	132905451.958	132905452.261	0.008	2.350
195.6	132905451.958	132905451.966	0.008	2.350
197.0	132905451.958	132905456.092	0.008	2.350
196.0	132905451.958	132905450.787	0.008	2.350

Table 3: The detailed list containing the offset time of the MRTOF-Ms t_0 with the masses of Ceasium-133 ($^{133}Cs^{+}$). The theoretical mass m_{AME} and the experimental mass m_{EXP} and their respective uncertanities are included.

B Raw data of Mass Measurement Accuracy

The following table presents the raw data obtained from the mass measurement accuracy experiment. The corresponding figures illustrate the ion time-of-flight (TOF) peaks. The numerical results extracted through graphical analysis are summarised in the table below.

Species	**A/q**	m_{AME} (μ **u**)	m_{EXP} (μ**u**)	Δm_{AME} (μ**u**)	Δm_{EXP} (μ**u**)	**Counts**
CO_2^+	44	43.9898292	43.989896116	0.00064	1.855	6800
Sr-94^{2+}	47	93.915355641	93.915501929	1.785	4.898	1001
Mo-100^{2+}	50	99.90746782	99.907637075	0.322	14.199	102
Zr-100^{2+}	50	99.918010499	99.91818207	8.742	8.496	2662
Cr-53^+	53	52.940646304	52.9407539	0.124	17.6	53
Tc-106^{2+}	53	105.914356674	105.914598549	13.15	11.805	419
Mo-106^{2+}	53	105.918273231	105.918451689	9.801	9.097	1044
Fe-56^+	56	55.934935537	55.935005743	0.287	9.149	1680
Pd-112^{2+}	56	111.907330557	111.907484556	7.027	14.779	92
Ru-112^{2+}	56	111.918806922	111.918955273	10.305	12.993	194
Sb-132^{2+}	66	131.914508013	131.914709794	2.648	22.81	417
Sn-132^{2+}	66	131.917823898	131.917988511	2.121	15.396	1180
CF_3^+	69	68.9952095	68.995284688	0.264	1.892	1185
Ce-150^{2+}	75	149.930384032	149.930541855	12.556	5.302	1215
Pr-150^{2+}	75	149.926676391	149.926845264	9.677	9.185	414
Kr-80^+	80	79.91637794	79.916418029	0.745	3.568	974
Kr-84^+	84	83.91149772708	83.911529963	0.0041	2.266	1114
Kr-86^+	86	85.91061062468	85.910641374	0.00399	3.088	681
Rb-87^+	87	86.909195009	86.909206348	0.006	3.774	1078
Rb-95^+	95	94.929263849	94.929260075	21.733	18.745	24
Mo-105^+	105	104.916981989	104.917018766	9.721	8.64	92
Ru-110^+	110	109.914038501	109.914070919	9.58	6.924	183
Cs-133^+	133	132.905451958	132.905450198	0.008	27.032	3549

Table 4: The detailed list of mass measurements of various ions or molecules with different mass-to-charge ratios A/q. The table contains theoretical AME mass m_{AME} and its uncertainty Δm_{AME} [7] in atomic mass unit (u), experimental mass m_{EXP} and its uncertainty Δm_{EXP} in atomic mass unit (u) and the counts recorded per ion or molecule.

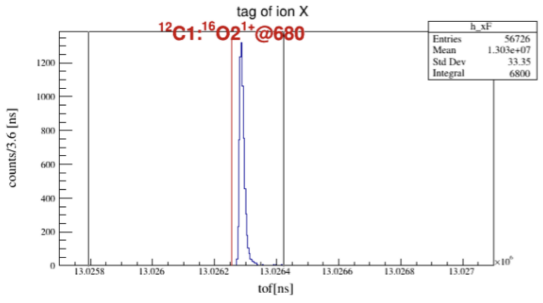

(a) The overview of measured ions for fitting.

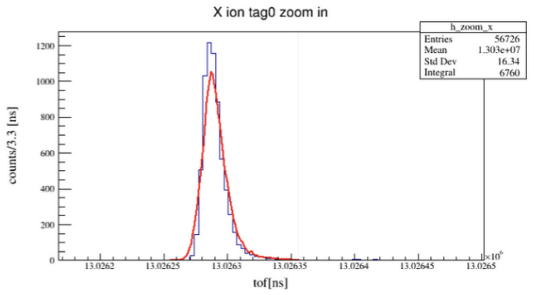

(b) Fitted peak of CO_2^+.

Figure 10: Figures above show the peaks measured of mass-to-charge ratio A/q=44. Subfigure (**a**) shows all the peaks available. Subfigure (**b**) shows the fitted peak of CO_2^+.

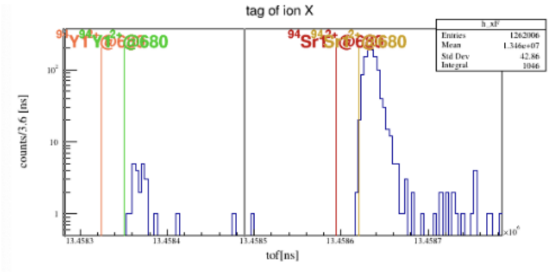

(a) The overview of measured ions for fitting.

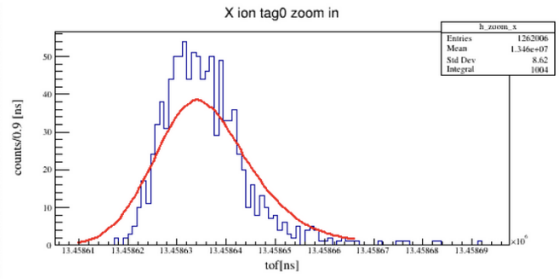

(b) Fitted peak of $^{94}Sr^{2+}$.

Figure 11: Figures above show the peaks measured of mass-to-charge ratio A/q=47. Subfigure (**a**) shows all the peaks available. Subfigure (**b**) shows the fitted peak of $^{94}Sr^{2+}$.

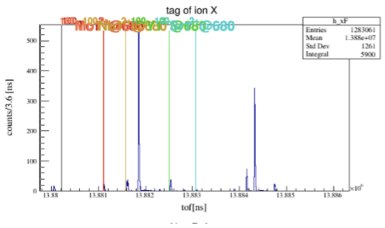

(a) The overview of measured ions for fitting.

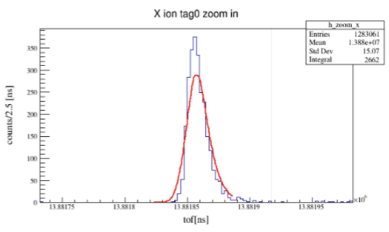

(b) Fitted peak of $^{100}Zr^{2+}$.

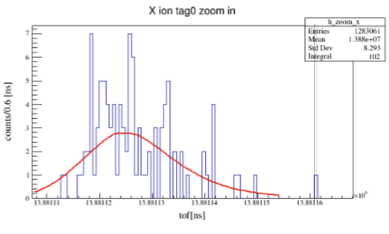

(c) Fitted peak of $^{100}Mo^{2+}$.

Figure 12: Figures above show the peaks measured of mass-to-charge ratio A/q=50. Subfigure (**a**) shows all the peaks available. Subfigure (**b**) shows the fitted peak of $^{100}Zr^{2+}$. Subfigure (**c**) shows the fitted peak of $^{100}Mo^{2+}$.

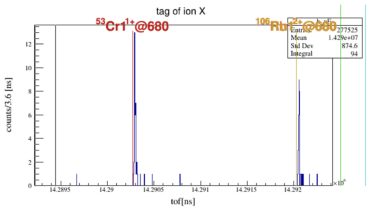

(a) The overview of measured ions for fitting.

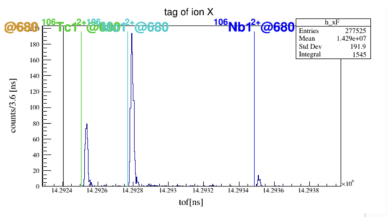

(b) The overview of measured ions for fitting.

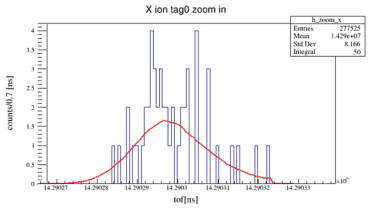

(c) Fitted peak of $^{53}Cr^{1+}$.

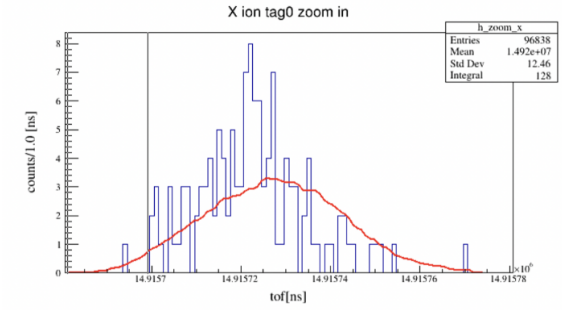

(d) Fitted peak of $^{106}Mo^{2+}$.

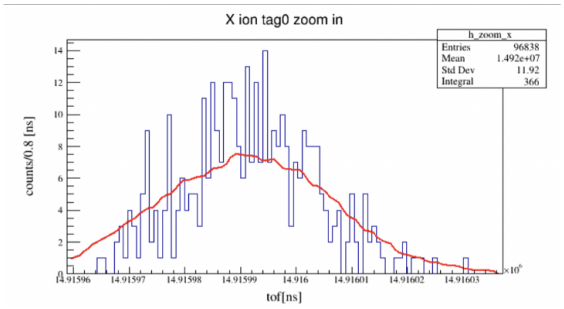

(e) Fitted peak of $^{106}Tc^{2+}$.

Figure 13: Figures above show the peaks measured of mass-to-charge ratio A/q=53. Subfigures (**a**) and (**b**) show all the peaks available. Subfigure (**c**) shows the fitted peak of $^{53}Cr^{1+}$. Subfigure (**d**) shows the fitted peak of $^{106}Mo^{2+}$. Subfigure (**e**) shows the fitted peak of $^{106}Tc^{2+}$.

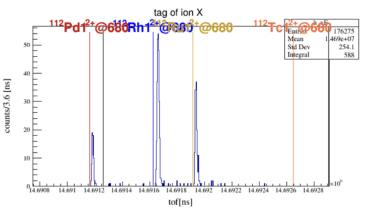

(a) The overview of measured ions for fitting.

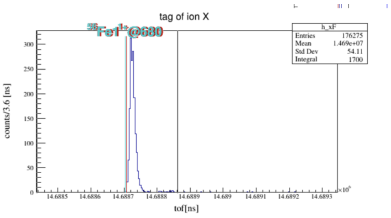

(b) The overview of measured ions for fitting.

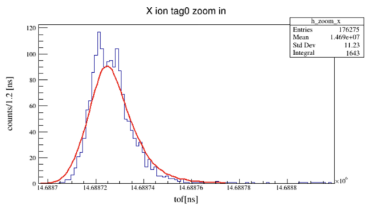

(c) Fitted peak of $^{56}Fe^{1+}$.

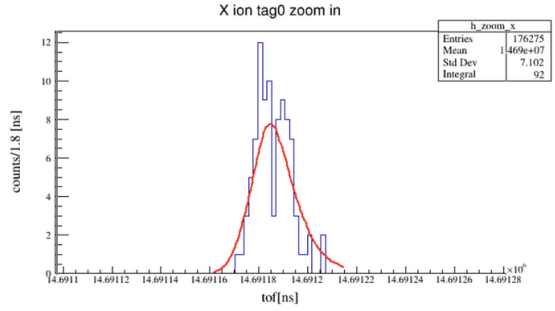

(d) Fitted peak of $^{112}Pd^{2+}$.

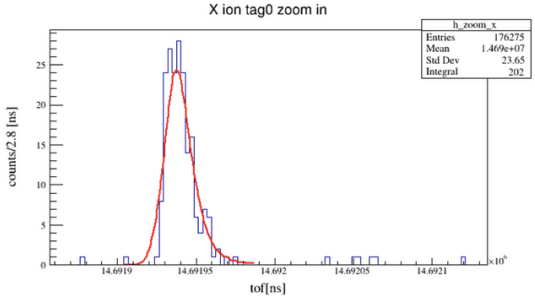

(e) Fitted peak of $^{106}Ru^{2+}$.

Figure 14: Figures above show the peaks measured of mass-to-charge ratio A/q=56. Subfigures (**a**) and (**b**) show all the peaks available. Subfigure (**c**) shows the fitted peak of $^{56}Fe^{1+}$. Subfigure (**d**) shows the fitted peak of $^{112}Pd^{2+}$. Subfigure (**e**) shows the fitted peak of $^{112}Ru^{2+}$.

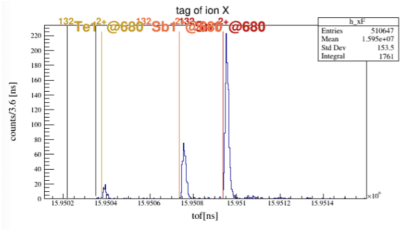

(a) The overview of measured ions for fitting.

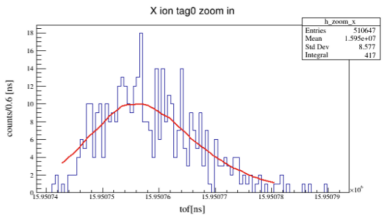

(b) Fitted peak of $^{132}Sb^{2+}$.

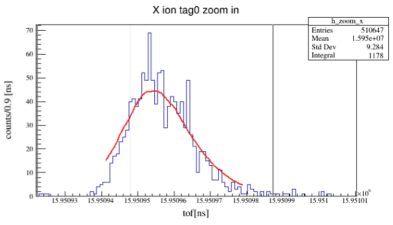

(c) Fitted peak of $^{132}Sn^{2+}$.

Figure 15: Figures above show the peaks measured of mass-to-charge ratio A/q=66. Subfigure (**a**) shows all the peaks available. Subfigure (**b**) shows the fitted peak of $^{132}Sb^{2+}$. Subfigure (**c**) shows the fitted peak of $^{132}Sn^{2+}$.

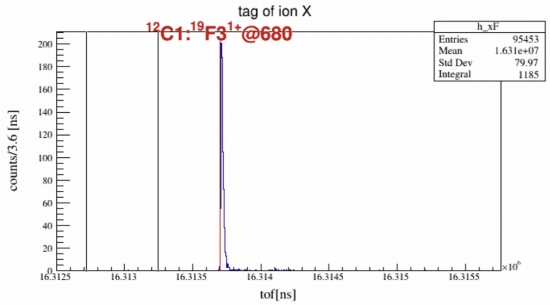

(a) The overview of measured ions for fitting.

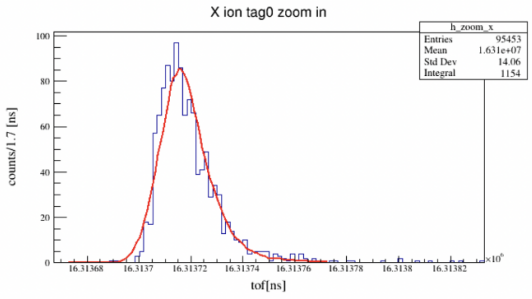

(b) Fitted peak of CF_3.

Figure 16: Figures above show the peaks measured of mass-to-charge ratio A/q=69. Subfigure (**a**) shows all the peaks available. Subfigure (**b**) shows the fitted peak of CF_3.

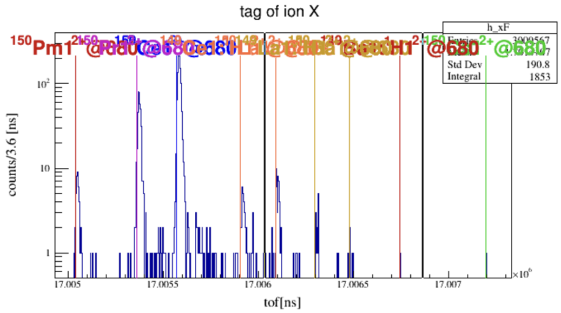

(a) The overview of measured ions for fitting.

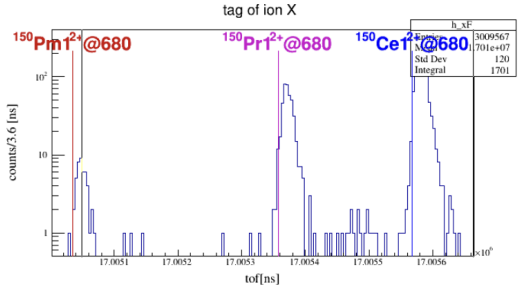

(b) The overview of measured ions for fitting.

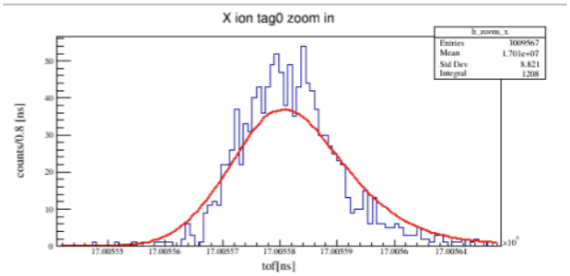

(c) Fitted peak of $^{150}Ce^{2+}$.

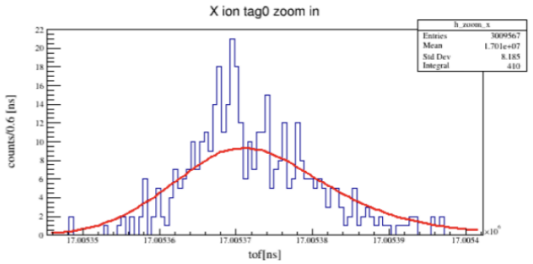

(d) Fitted peak of $^{150}Pr^{2+}$.

Figure 17: Figures above show the peaks measured of mass-to-charge ratio A/q=75. Subfigures (**a**) and (**b**) show all the peaks available. Subfigure (**c**) shows the fitted peak of $^{150}Ce^{2+}$. Subfigure (**d**) shows the fitted peak of $^{150}Pr^{2+}$.

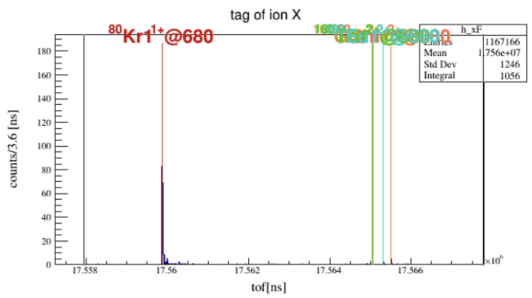

(a) The overview of measured ions for fitting.

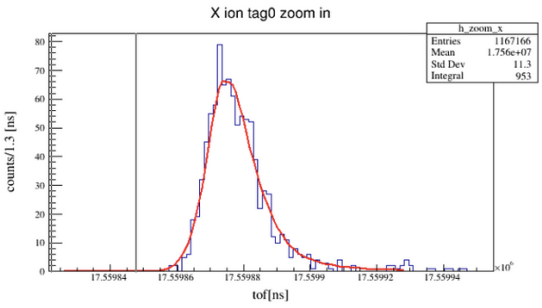

(b) Fitted peak of $^{80}Kr^{1+}$.

Figure 18: Figures above show the peaks measured of mass-to-charge ratio A/q=80. Subfigure (**a**) shows all the peaks available. Subfigure (**b**) shows the fitted peak of $^{80}Kr^{1+}$.

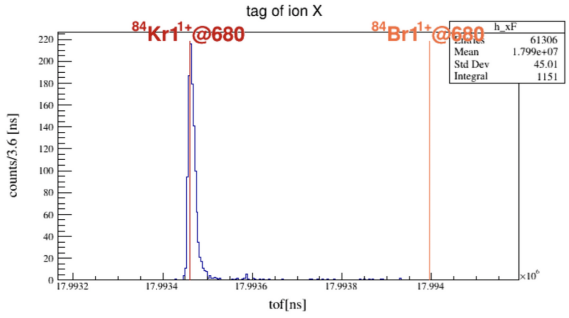

(a) The overview of measured ions for fitting.

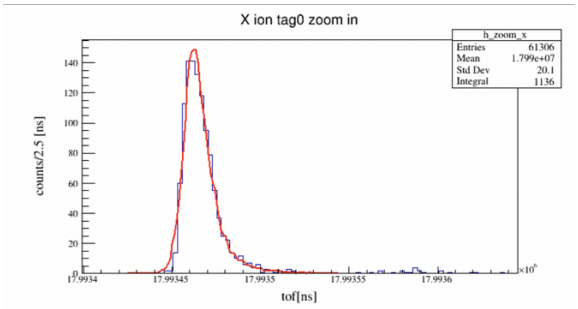

(b) Fitted peak of $^{84}Kr^{1+}$.

Figure 19: Figures above show the peaks measured of mass-to-charge ratio A/q=84. Subfigure (**a**) shows all the peaks available. Subfigure (**b**) shows the fitted peak of $^{84}Kr^{1+}$.

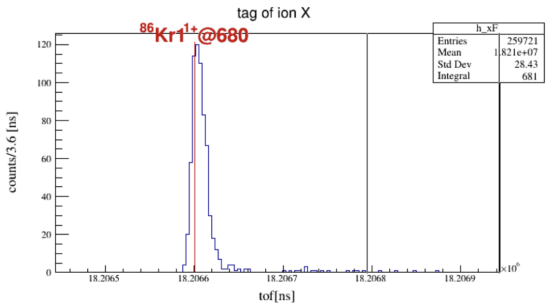

(a) The overview of measured ions for fitting.

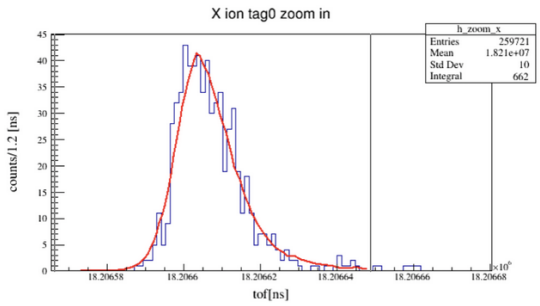

(b) Fitted peak of $^{86}Kr^{1+}$.

Figure 20: Figures above show the peaks measured of mass-to-charge ratio A/q=86. Subfigure (**a**) shows all the peaks available. Subfigure (**b**) shows the fitted peak of $^{86}Kr^{1+}$.

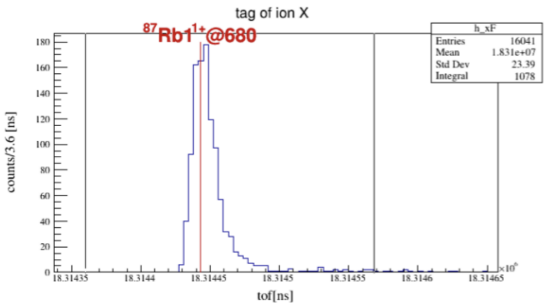

(a) The overview of measured ions for fitting.

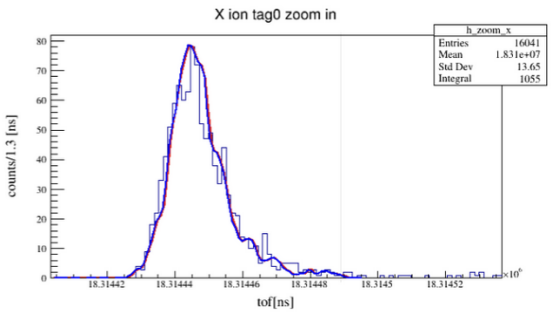

(b) Fitted peak of $^{87}Rb^{1+}$.

Figure 21: Figures above show the peaks measured of mass-to-charge ratio A/q=87. Subfigure (**a**) shows all the peaks available. Subfigure (**b**) shows the fitted peak of $^{87}Rb^{1+}$. Special fitting methods were used due to the low count number.

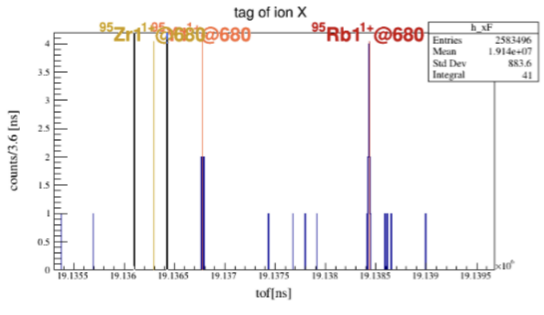

(a) The overview of measured ions for fitting.

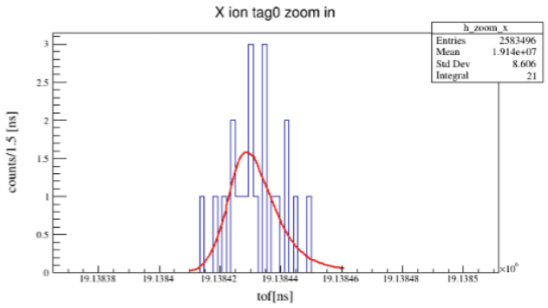

(b) Fitted peak of $^{95}Rb^{1+}$.

Figure 22: Figures above show the peaks measured of mass-to-charge ratio A/q=95. Subfigure (**a**) shows all the peaks available. Subfigure (**b**) shows the fitted peak of $^{95}Rb^{1+}$.

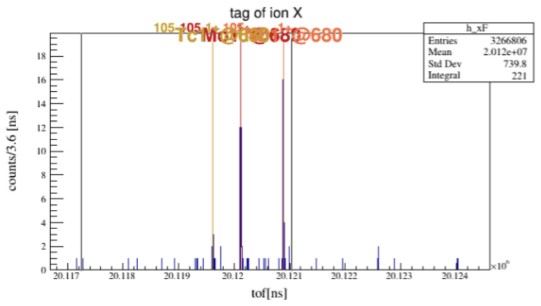

(a) The overview of measured ions for fitting.

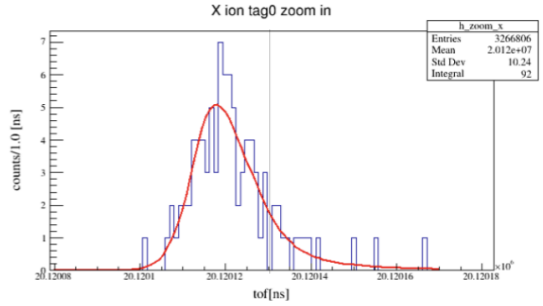

(b) Fitted peak of $^{105}Mo^{1+}$.

Figure 23: Figures above show the peaks measured of mass-to-charge ratio A/q=105. Subfigure (**a**) shows all the peaks available. Subfigure (**b**) shows the fitted peak of $^{105}Mo^{1+}$.

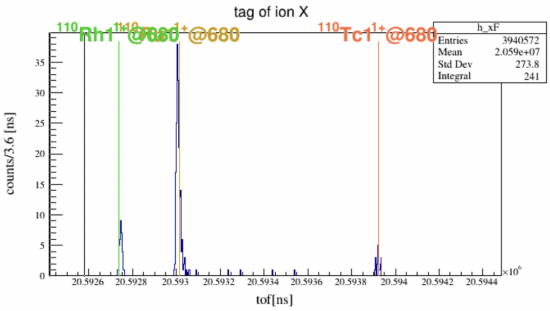

(a) The overview of measured ions for fitting.

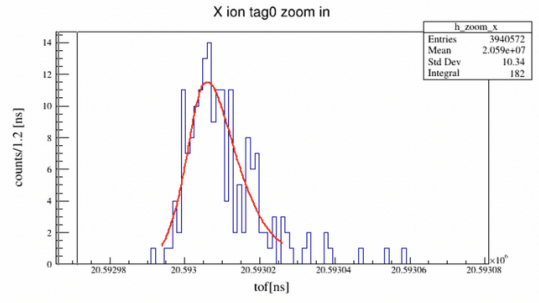

(b) Fitted peak of $^{110}Ru^{1+}$.

Figure 24: Figures above show the peaks measured of mass-to-charge ratio A/q=110. Subfigure (**a**) shows all the peaks available. Subfigure (**b**) shows the fitted peak of $^{110}Ru^{1+}$.

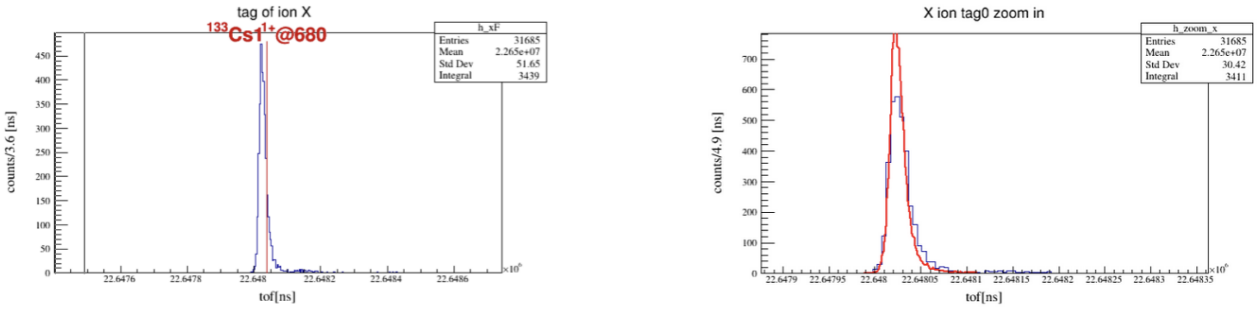

(a) The overview of measured ions for fitting.

(b) Fitted peak of $^{133}Cs^{1+}$.

Figure 25: Figures above show the peaks measured of mass-to-charge ratio A/q=133. Subfigure (**a**) shows all the peaks available. Subfigure (**b**) shows the fitted peak of $^{133}Cs^{1+}$.